Role of nanoscale defect features in enhancing the thermoelectric performance of p-type nanostructured SiGe alloys

Sivaiah Bathula,[1,2] M. Jayasimhadri[2], Bhasker Gahtori[1], Niraj Kumar Singh[1],
Kriti Tyagi[1,3], A. K. Srivastava[1] and Ajay Dhar[1,*]

[1] *CSIR-Network of Institutes for Solar Energy, CSIR-National Physical Laboratory, Dr. K. S. Krishnan Road, New Delhi -110012, India*
[2] *Department of Applied Physics, Delhi Technological University, Delhi, India*
[3] *Acdemy of Scientific and Innovative Research (AcSIR), CSIR-National Physical laboratory (NPL) Campus, New Delhi, India*

Abstract

Despite SiGe being one of the most widely studied thermoelectric material owing to its application in radioisotope thermoelectric generators (RTG), the thermoelectric figure-of merit (ZT) of p-type SiGe is still quite low resulting in poor device efficiencies. In the present study, we report a substantial enhancement in ZT ~ 1.2 at 900°C for p-type nanostructured $Si_{80}Ge_{20}$ alloys by creating several types of defect features within the $Si_{80}Ge_{20}$ nanostructured matrix, in a spectrum of nano to meso-scale dimensions, during its nanostructuring, employing mechanical alloying followed by spark plasma sintering. This enhancement in ZT, which is ~ 25% over the existing state-of-the-art value for p-type nanostructured $Si_{80}Ge_{20}$ alloy, is primarily due to its ultralow thermal conductivity ~ 2.04 W/mK at 900°C, resulting from the scattering of low-to-high wavelength heat-carrying phonons by different types of defect features in a range of nano to meso-scale dimensions in the $Si_{80}Ge_{20}$ nanostructured matrix. These include point defects, dislocations, isolated amorphous regions, nano-scale grain boundaries and more importantly the nano to meso-scale residual porosity distributed throughout the $Si_{80}Ge_{20}$ matrix. These nanoscale multi-dimensional defect features have been characterized employing scanning and transmission electron microscopy and correlated with the electrical and thermal transport properties, based on which the enhancement of ZT has been discussed.

Keywords: $Si_{80}Ge_{20}$ nanostructured alloys, thermoelectrics, nanostructuring, spark plasma sintering, figure-of-merit

---

[*] Corresponding author: adhar@nplindia.org
Tel.: +91 11 4560 9456; Fax: +91 11 4560 9310

1. Introduction

The direct conversion of heat into electricity based on thermoelectric (TE) effect is an eco-friendly alternative for power generation due to the fast depleting fossil fuels[1] coupled with growing concerns for environmental pollution.[2] With the advent of efficient thermoelectric materials the thermoelectric power generation technology is gradually evolving as a suitable alternative to the other existing renewable sources of energy.[3] The performance of a TE material is mainly judged by its dimensionless figure-of-merit (ZT) defined as[4], $ZT = \alpha^2\sigma T/(\kappa_e + \kappa_L)$, where α, σ, and T are the Seebeck coefficient, electrical conductivity, and absolute temperature, respectively and κ_e and κ_L are the electronic and lattice contribution to the thermal conductivity (κ).

Currently, there are a host of TE materials available with relatively high ZT, in the low to intermediate temperature range, which include several, tellurides[5], selenides[6], skutterudites[7] and several other complex alloys[8]. However, very few TE materials are currently available for high temperature (~900°C) TE applications, which include $Si_{80}Ge_{20}$,[4, 9, 10] $Yb_{14}MnSb_{11}$,[11] $Ba_8Ga_{16}Ge_{30}$,[12] $Hf_{0.75}Zr_{0.25}NiSn$[13] etc. Most of these TE materials either posses a low ZT or do not have a compatible n/p counterpart required for TE device fabrication. Nevertheless, among these, SiGe alloys are a unique class of material, which are chemically stable at high temperatures, possess high mechanical strength coupled with a reasonably high ZT and can also be synthesized as n or p-type by suitable doping. Due to these unique characteristics, SiGe alloys are one of the most widely studied TE materials for power generation and are being successfully used in Radioisotope TE Generators (RTGs) in spacecrafts for remote terrestrial and extraterrestrial deep space missions since 1976.[4, 10, 14]

During nearly past four decades, many researchers[4, 10, 15-18] have attempted to enhance the ZT of both n and p-type SiGe alloys by employing various material processing methodologies using different dopants. However, most of these studies are based on n-type SiGe[15] as it is rather difficult to improve the ZT of its p-type counterpart due to the lower mobility of holes as compared to electrons.[10] The earliest study on bulk p-type SiGe alloy[4, 10] reported a peak ZT of 0.5 at 900°C, which was later enhanced to 0.65[4, 10] and these are currently being employed in RTGs for power generation. However, a drastic increase in ZT was reported by employing the revolutionary concept of "nanostructuring", which led to a "*phonon glass-electron crystal*" type of behavior in SiGe nano-alloys.[19] Employing this strategy of nanostructuring, comprising of high energy ball milling (HEBM) followed by hot pressing, a ZT of 0.95[9] at 900°C was reported for p-type $Si_{80}Ge_{20}$ nanostructured alloys and this value has remained the highest reported since 2008. Employing a similar strategy, the authors have earlier report a record value of ZT ~ 1.5 for n-type nanostructured SiGe alloys using spark plasma sintering of mechanically alloyed elemental nanopowders.[15]

Despite their active usage in RTGs for nearly four decades, the TE conversion efficiency (η) of SiGe based devices is still quite low ~ 5-7%.[3, 4] Among the several approaches reported for enhancing the ZT (and thus η), reducing κ_L has been found to be the most plausible strategy, as κ_e is coupled to σ through the Wiedmann-Franz law.[20] Since both σ and κ are intimately related to the microstructure of the material, one way to improve ZT is *via* "nanostructuring",[19, 21-24] which allows reduction in κ_L[25] without significantly affecting the power factor ($S^2\sigma$). This strategy has been earlier successfully demonstrated on several nanostructured TE alloys and compounds[2, 15, 19, 21, 26-29] and the enhancement in ZT, in some cases has been reported to be as high six fold[19] over their bulk counterpart. The enhancement due to nanostructuring is attributed primarily to the scattering of heat-carrying phonons by high density of nano-scale grain boundaries leading to a decrease in κ.

There are several theoretical[29-33] and experimental[34-37] studies in the literature on TE materials including Si[26, 38] and SiGe,[30, 39] reporting a considerable enhancement in ZT due to nano-porosity, which is primarily due to the scattering of heat-carrying phonons by these nano-sized pores leading to a reduction in κ. These results show that the degradation in σ due to the presence of nano-pores is more than compensated by a large reduction in κ_L, resulting in a significantly enhanced ZT. Recently a panoscopic approach[29, 40, 41] for the enhancement of ZT in TE materials has been proposed by He et al.[30] and Biswas et al.[40] by introduction of different dimensional atomic (point defects), nano (line and interfacial defects) and meso-scale (nano-precipitate grain boundaries) features, which contribute to the scattering in a large spectrum of short-to-long wavelength heat-carrying phonons. Employing this all length-scale hierarchical structuring approach they have reported a high ZT ~ 2.3 in PbTe with 4 mol% SrTe nano-precipitates.[40]

In the present study, we have employed a similar panoscopic all length-scale hierarchical structuring approach[40, 41] for enhancing ZT in nanostructured p-type SiGe, except that we have introduced controlled nanoporosity as the nano to meso-scale defect feature in the nanostructured SiGe matrix, and these nanoscale pores act as additional scattering centers for heat-carrying phonons. This approach for obvious reasons is simple, as the size and distribution of nano to meso-scale porosity in the TE material matrix can be conveniently engineered experimentally[20, 34, 36, 42] by optimizing the process parameters of spark plasma sintering (SPS) to match the wavelength range of the phonons to be scattered. Further, apart from residual porosity, the other atomic and nano-scale defect features like, dislocations and nanoscale grain boundaries are also introduced in SiGe nanostructured matrix during its powder metallurgy processing[19, 43, 44] employing high energy ball milling (HEBM) followed by SPS at optimized process parameters. SPS, apart from retaining these nanoscale features,[15, 45] which were created during HEBM, it has also aids in the creation of a distributed nano to meso-scale residual porosity in the SiGe nanostructured matrix.[35, 46] The overall effect of these nano to meso-scale defect features leads to an abundant scattering of low-to-high wavelength phonons resulting in a very small value of $\kappa \sim 2.04\ Wm^{-1}K^{-1}$ (at 900°C) which in turn enhances the ZT.

2. Experimental procedure

Si (99.99%), Ge (99.99%) and B (99.99%) powders all from M/s. Alfa Aesar, USA were taken in chemical stoichiometric proportion and mechanically milled in a high energy ball mill *(Fritsch, Pulverisette-4)* for an optimized time period of 90 hours. The grinding bowls and balls were made of hardened stainless steel. The ball-to-powder weight ratio was optimized at 20:1 and the process was carried out in an argon atmosphere with a speed of 400 rpm. In order to prevent re-welding and to promote fracturing of powder particles, 2 wt.% of stearic acid was added as a process control agent[15]. Prior to sintering, the processing of the high energy ball milled alloy powders was carried out in a glove box *(Mbraun, MB20)* to avoid oxidation and other atmospheric contamination. Phase identification and crystallite size determination was carried out by x-ray powder diffraction *(Rigaku,* 40kV and 30 mA) analysis. The nanostructured alloy powders were subsequently consolidated and sintered under vacuum (~4 Pa) using spark plasma sintering *(SPS Syntex, 725)* at an optimized pressure of 60 MPa at temperatures ranging from 900 to 1150°C with a soaking time of 3 minutes. SPS heating rate of 400°C/minute was maintained for all sintering experiments which were carried out in graphite die and punches to obtain circular disks of size ~12.7 mm diameter. The actual composition of nanostructured sintered SiGe samples was determined using Flame atomic absorption spectrometry and EDS (Energy Dispersive Spectroscopy) techniques (Analytik Jena, Vario-6) and they exhibited almost the same stoichiometry as the starting composition, with no evidence of any Fe contamination.

Lattice scale images have been recorded using High resolution transmission electron microscopy (HRTEM) *(Tecnai G2 F30 STWIN)* operated at an electron accelerating voltage of 300 kV using field emission gun as an electron source. Specimens for electron microscopy were prepared by employing mechanical polishing followed by subsequent ion milling. Mechanical polishing was finally carried out on the specimen of 3 mm diameter disc to 100 μm, further thickness was reduced to 20 to 30 μm by utilizing a dimple grinder *(515 CE, South Bay Technology)*. Subsequently ion beam milling was carried out using an ion milling system *(Baltec RES 101)* at 7 kV and low angle milling to have an ultimate perforation to make the specimen transparent to the electron beam. During ion milling, Ar^+ ions were used for gentle thinning of the specimen without any damage for few minutes. Field Emission Scanning Electron Microscope (FESEM) (*Zeiss, Supra 40VP)* was used to study the morphology of the sintered samples. For thermal diffusivity measurements, the as-sintered circular disc specimen of 12.7 mm diameter were used for measurement using a laser flash system *(Laser Flash Analyzer, LFA 10000)*. The specific heat was measured by using differential scanning calorimeter (*Netzsch, DSC 404 F3*) and density using conventional Archimedes principle. The thermal conductivity (κ) was calculated from the product of thermal diffusivity (D), specific heat capacity (C_p), and density (d), expressed as $\kappa = D \times C_p \times d$. For the electrical transport measurements, rectangular samples of dimensions 12 x 3 x 3 mm^3 were employed and the Seebeck coefficient and electrical conductivity were measured by four probe DC method in helium atmosphere *(ZEM-3, Ulvac Inc., Germany)*. The accuracies in transport measurement are: ± 6% for thermal diffusivity, ± 7% for electrical conductivity, ± 7% for Seebeck coefficient, ± 5% for specific heat and ± 0.5% for density.

3. Results and Discussion

3.1 X-Ray diffraction

Figure 1(a) shows the XRD patterns of un-milled starting elemental powders, mechanically alloyed nanopowders ball milled for 90 h and nanostructured $Si_{80}Ge_{20}$ alloys spark plasma sintered at various temperatures. It is apparent from this figure that after 90 h of ball-milling

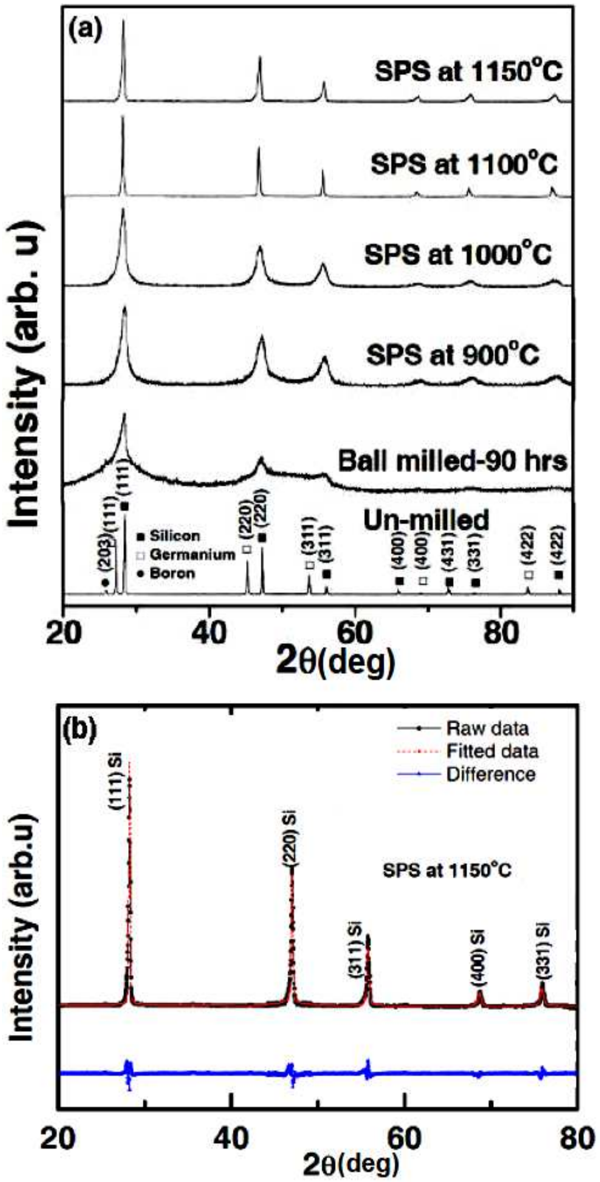

Fig. 1: *(Color online)* XRD of p-type $Si_{80}Ge_{20}$ nanostructured alloy (a) Un-milled powders, ball milled for 90 hours and SPS at various temperatures (b) Rietveld refinement of XRD data of nanostructured $Si_{80}Ge_{20}$ alloy sintered at 1150°C. The red, black and blue lines indicate the observed, fitted and observed minus fitted data, respectively.

Ge completely dissolves in the Si matrix and the XRD peaks exhibit a significant broadening. This peak broadening is attributed to nanostructuring as well as a considerable amount of strain in the nanopowders, due to the impact and shear forces of milling media during HEBM.[9, 18, 47] It is also clear from these XRD patterns that the $Si_{80}Ge_{20}$ phase, formed during HEBM, is maintained even after SPS at the highest temperature of 1150ºC. Reitveld refinement of the XRD data of nanostructured $Si_{80}Ge_{20}$ alloy sintered at 1150ºC (Fig. 1(b)) exhibited a diamond-like cubic structure with space group $Fd\bar{3}m$ and lattice constant of 5.47 Å, which is in perfect agreement with that calculated using the modified Vegard's law.[48] Fig. 2 (a) shows the dependence of the average crystallite size and lattice strain in nanostructured $Si_{80}Ge_{20}$ alloys on the SPS temperature, determined employing Williamson-Hall method[49], using the XRD data from Fig.1 after correcting the instrumental broadening.

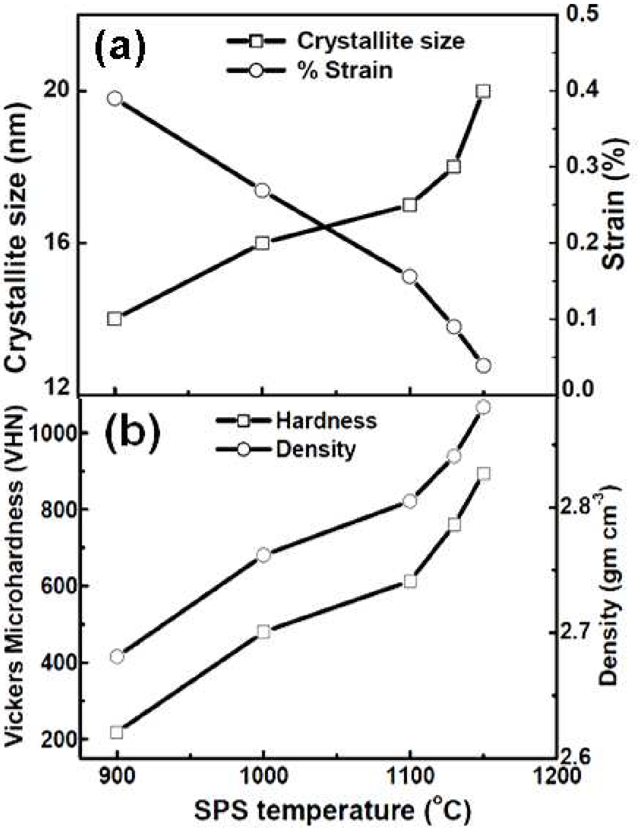

Figure 2: SPS temperature dependence of nanostructured $Si_{80}Ge_{20}$ alloys on **(a)** crystallite size and % Strain and **(b)** Vickers micro-hardness and bulk density

Figure 2 suggests that the average crystallite size of $Si_{80}Ge_{20}$ nanopowders, after 90 h of HEBM was found to be ~13 nm which gradually coarsened up with increasing SPS temperature and at 1150°C it was estimated to be ~20 nm. Expectedly, the lattice strain shows a sharp fall with increasing SPS temperature and at 1150°C the sample was nearly in strain-free condition. Fig. 2(b) shows that, expected, the bulk density also increases with increasing SPS temperature and finally attains a value of 2.88 gm/cc at 1150°C. Further, it is also evident from Fig. 2(b) that the Vickers micro-hardness of SiGe nanostructured alloy increases with increasing SPS temperature and for samples sintered at 1150°C it exhibits a high value of 9 GPa, which is comparable to other state-of-the-art TE materials[50]. Beyond 1150°C, the incipient melting of SiGe particles was observed, which leads to a drastic increase in their crystallite size. Thus, a sintering temperature of 1150°C was optimized for all SPS experiments at which the nanostructured $Si_{80}Ge_{20}$ alloys exhibited a density of 98.3% of its theoretical density.

3.2 Microstructural Analysis

The HRTEM image of the HEBM $Si_{80}Ge_{20}$ nanopowders, shown in Fig. 3(a), exhibits agglomerated nano-grained SiGe particles in a range of 50 - 300 nm. However, a corresponding high magnification atomic scale image, shown in Fig. 3(b), clearly reveals randomly oriented individual nanocrystallites in the range of ~ 9 - 14 nm with an average crystallite size of ~12 nm, which is close to that estimated from XRD analysis. The FESEM image of the sintered SiGe nanostructured sample, shown in Fig. 4(a & b), exhibited a uniform microstructure with nanocrystalline aggregates and a residual porosity of varying nano-to-meso scale dimensions (~25 to 200 nm) distributed throughout the matrix.[30-32, 36, 51-53] The size and distribution of these nano-pores can be controlled by the SPS processing parameters, mainly pressure[20, 42] and the volume fraction of stearic acid,[54] used as a process control agent during high energy ball milling, which evaporates at high temperatures during SPS leaving behind nanopores. These processing parameters were optimized to introduce controlled nano-to-meso scale porosity in the SiGe nanostructured matrix, which is dimensionally comparable to mid-to-high wavelength phonons responsible for maximum heat-transport.[26, 28] Similar nanoscale residual porosity has also been earlier reported in several TE materials[30-32, 36, 51-53] sintered employing SPS.

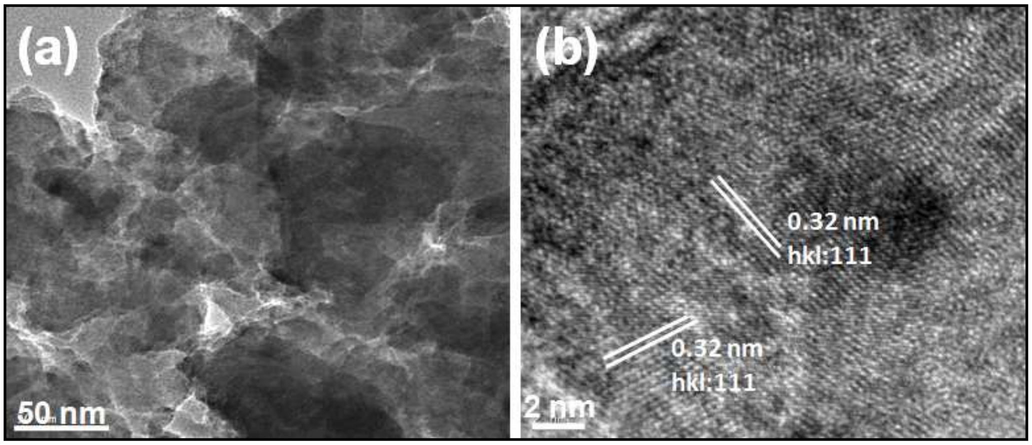

Figure 3 TEM images of $Si_{80}Ge_{20}$ nanostructured powder ball-milled for 90 hours showing (a) nanocrystalline aggregates of individual particles and (b) individual nanocrystallites with an inter-planar spacing of 0.32nm.

A detailed microstructural characterization of the nanostructured $Si_{80}Ge_{20}$ alloy samples employing HRTEM elucidated several interesting features in real and reciprocal space. A uniform microstructure was observed (Fig. 5a) with ultrafine-grains distributed throughout the microstructure. A small rectangular region (marked with white dotted line, Fig. 5a) is further magnified and displayed as the top-left inset in Fig. 5(a), which suggests that fine nano-scale grains of SiGe are distributed homogeneously in the microstructure. A corresponding EDS spectrum (top-right inset in Fig. 5(a)) exhibits the presence of major elemental peaks with chemical composition close to the starting stoichiometry. The atomic scale image in the bottom inset of Fig. 5(a) shows nanocrystallites of different sizes (separated by white dotted lines) randomly oriented with respect to one another. Fig. 5(b) shows the atomic scale image of nanostructured $Si_{80}Ge_{20}$ alloy typically exhibiting two well-oriented SiGe nanocrystallites with a clear interface, marked by a white dotted line. In general, these atomic scale images indicate that a major fraction of the SiGe matrix microstructure consists of different sized nanocrystallites randomly orientated with respect to each other with a dominance of crystallites oriented in 111 planes, which may be due to the density of particular set of planes with preferred growth during synthesis.

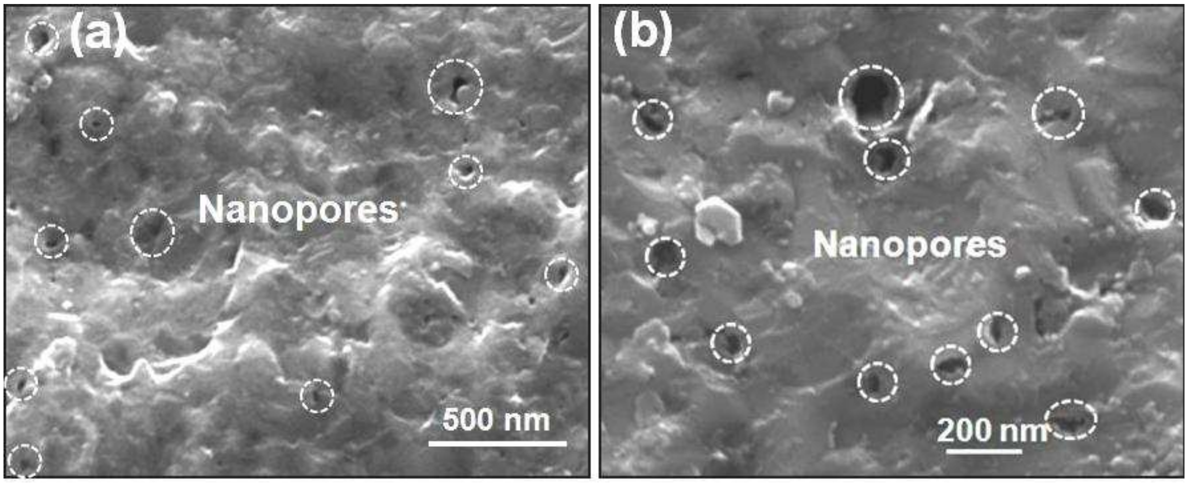

Figure 4 (a & b): FESEM images of nanostructured $Si_{80}Ge_{20}$ alloy showing nano to meso-scale pores in the size range ~ 25 – 200 nm distributed throughout the matrix.

Apart from SiGe nanocrystallites, some regions with perturbed atomic scale arrangement are also clearly evident in the lattice-scale images (encircled by white dotted lines and marked as A in Fig. 5 (b-d)), which may be attributed to a random coordination of the atoms in these regions leading to microstructural defects in a regular lattice structure. A corresponding FFT pattern, shown as an inset in Fig 5(b), depicts a diffused background in the centre, which corroborates the presence of microstructural lattice scale imperfections, generated due to extended duration of HEBM[2, 43, 55] and also due to sintering of these nanopowders at very high sintering rates during SPS.[15]

In Fig. 5(c), in addition to microstructural imperfections (marked as A), the atomic scale image of nanostructured $Si_{80}Ge_{20}$ alloy also shows a region comprising an amorphous structure (marked by a set of white dotted lines) along with few overlapped planes, leading to a mushy microstructure consisting of amorphous and crystalline planes of two different orientations. Further the inset in Fig 5 (c) represents a low magnification bright field micrograph of with two SiGe nano-grains separated by an amorphous grain boundary (marked by white arrows).

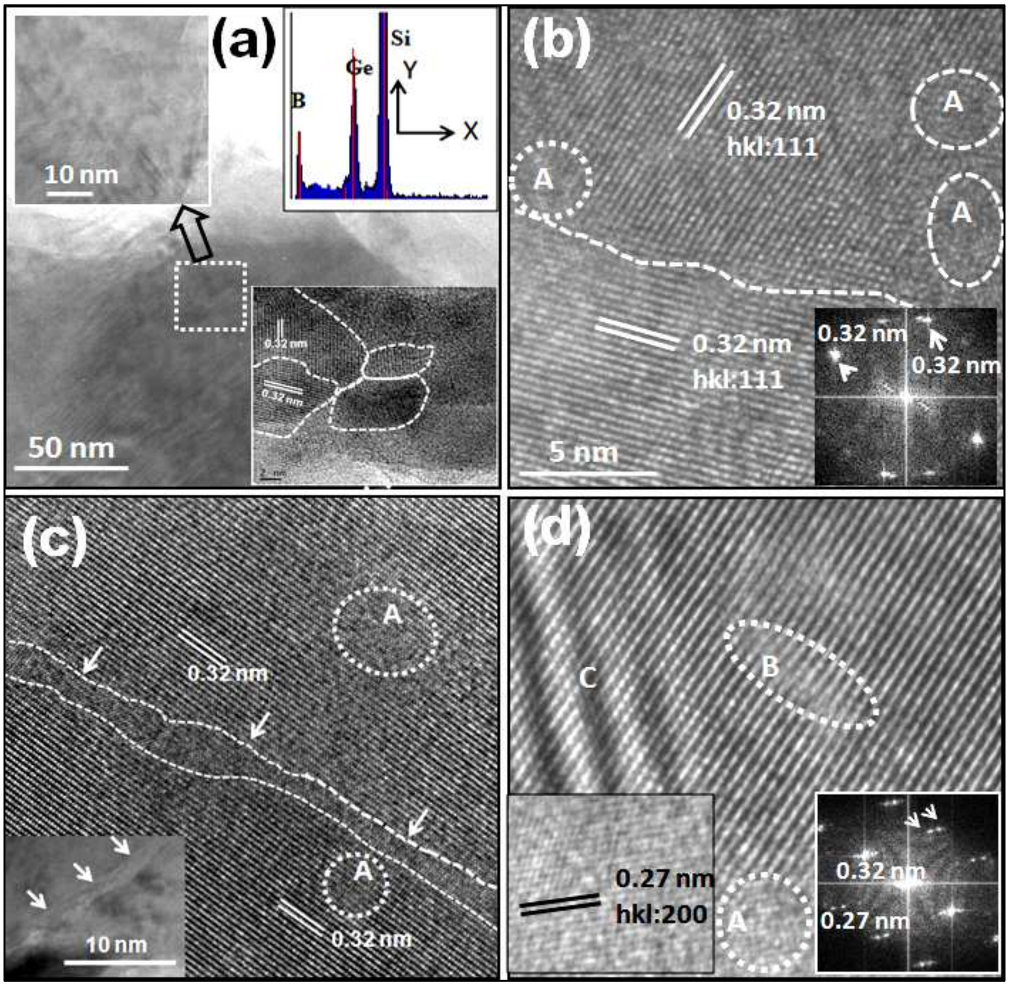

Figure 5: HRTEM images of nanostructured $Si_{80}Ge_{20}$ alloy, showing (a) *u*niform, ultra-fine and densely packed microstructure, (b) two orientations of 111 planes of a cubic crystal at an atomic scale; regions encircled as A are lattice scale imperfections, (c) white dotted interface region between two nanocrystallites comprising of an amorphous phase along with a few overlapped planes and region B showing a mushy microstructure of amorphous & crystalline planes of two different orientations, and (d) imperfections consisting of dislocations (marked as B) and micro-defect layers (marked as C) in the lattice. Insets in (a) fine grained microstructure (top-left); EDS pattern (top-left) with X-axis: keV, Y-axis: intensity (arb. units); distribution of randomly oriented nano-crystallites with boundaries marked with white dotted lines, (b) FFT revealing two variants of 111 plane, (c) bright field micrograph showing amorphous nanograin boundary (marked with white arrows) (d) FFT showing 111 and 200 planes.

The occurrence of amorphous regions at the grain boundaries is well known in nanostructured materials[43, 56, 57] synthesized using mechanical alloying, including pristine Si[58]. The HEBM followed by SPS, employed for the synthesis of nanostructured $Si_{80}Ge_{20}$ alloy, apart from leading to dense nano-grain boundaries also leads to several other lattice scale alterations in the microstructure. One such atomic scale feature in the SiGe nanostructured alloys are the imperfections in the form of dislocations (region marked as B in Fig. 5d) and irregular layered-like structure (region marked as C in Fig. 5d) clearly revealing lattice scale modulations due to residual strain which originate during the HEBM of elemental powders. The bottom-left inset in Fig. 5(d) further shows the presence of 200 planes with inter-planar spacing of 0.27 nm. A corresponding FFT (bottom-right inset in Fig. 5d) recorded from the atomic scale image of Fig. 5(d) delineates the presence of 111 and 200 planes with inter-planar spacing of 0.32 and 0.27 nm, respectively, in reciprocal space. The presence of splitting in diffraction spots, as marked by a set of arrows on the FFT image, further corroborates the existence of imperfections in the nanocrystalline SiGe matrix along certain crystallographic orientations. In general, the atomic scale images of nanostructured $Si_{80}Ge_{20}$ alloys exhibited regions with defect features of an embedded amorphous phase in a crystalline lattice and regions showing dislocations (edge-type in nature) and a mushy type of microstructure, consisting of amorphous and crystalline phases *(Supplementary Information, Fig.S1(a&b))*. These nano-sized defect features of varying dimensions significantly contribute towards reduction in the lattice thermal conductivity and will be discussed in section 3.3.

3.3 Thermal transport

The temperature dependence of thermal conductivity, calculated from the measured thermal diffusivity and specific heat capacity data *(Supplementary Information, Fig. S2)* of our nanostructured SiGe alloy, has been displayed in Fig. 6(a), which suggests a behavior very close to that reported earlier by Joshi et al.[9] for nanostructured alloys with similar composition, but with a lower magnitude of ~ 2.04 $Wm^{-1}K^{-1}$ at 900°C, which is attributed to an abundant scattering of phonons in a wide wavelength range by atomic, nano and meso-scale defects.[28, 59, 60] This value of κ is the lowest reported thus far for p-type $S_{80}Ge_{20}$ and is ~ 50% lower than reported for the RTG bulk alloy[4, 10] and ~ 20% lower than the nanostructured alloys of similar composition.[9] It may be noted that compared to the nanostructured SiGe alloys, the bulk RTG counterpart, apart from the expectedly higher magnitude, exhibits an opposite nature of temperature dependence of κ. In general, the main operating phonon scattering mechanisms include, phonon-defects,[61, 62] phonon-phonon[63, 64] and Umklapp scattering[65] with the later generally dominant at high temperatures. As the mean-free-path of the acoustic phonons in bulk RTG sample is much larger than its nanostructured counterpart, due to existence of different kinds of defect features, in a range of nano-to-meso scale dimensions, which leads to the different nature of temperature dependence of κ.[10] However, at high temperatures (> 700°C), the increase in κ in bulk RTG SiGe alloys is attributed to the bipolar effect.[10, 66] On the other hand in nanostructured samples, the carriers are dominantly scattered by nano-scale defects whereas at higher temperatures these charge carriers are dominantly scattered by acoustic phonons.[17]

The κ comprises of contributions from both lattice (κ_L) and electronic (κ_e) part with κ_e being related to σ through the Wiedemann–Franz law[67], $\kappa_e = L\sigma T$. Accordingly, κ_L was calculated by subtracting κ_e from κ, considering the Lorenz number (L) for SiGe as 2.14 x 10^{-8} $W\Omega K^{-2}$ at room temperature[9, 15] and Fig. 6(b) shows the calculated temperature dependence of κ_L. It is well known that in SiGe bulk alloys[10] the main contribution to κ is primarily from the κ_L[4, 56, 68] rather than κ_e. However, κ_L being the contribution due to phonons, it can greatly be reduced by scattering by different kinds of atomic, nano or meso-scale defects,[28, 59, 60] the size of which is smaller than the mean free path of heat-carrying phonons in SiGe.[69-71] The phonons, in general, have a large spectrum of wavelengths with different wavelengths contributing different amounts to the effective heat conduction. However, it has been reported for several thermoelectric materials including Si,[26] PbTe,[39] PbTeSe[41] that about half of the contribution to κ_L is by phonon modes with mean free path between 5 and 100 nm (mid wavelength phonons), with rest of the contribution coming almost equally from phonons modes in the low (< 5 nm) and high (> 100 nm) spectrum of mean free paths.[32] In SiGe alloys, the short wavelength phonons are known to be scattered by point defects (impurity atoms) due to alloying[69] and the κ has been reported to be the lowest in the alloying range of 12-70% Ge in Si and remains constant throughout this alloying range.[70] This suggests that 20% alloying of Ge in Si is good enough to attain the maximum reduction in κ due to solid solution alloying,[28] as is the case in our $Si_{80}Ge_{20}$ nanostructured alloys. However, a significant reduction in κ_L can further be realized by increasing the phonon scattering by defects/disorder in nano to meso-scale, which has dimensional compatibility with that of the size of the wavelength of phonons, responsible for most of the heat conduction.[70, 72, 73]

The microstructural features of nanostructured $Si_{80}Ge_{20}$ alloys, delineated employing FESEM, HRTEM, (Fig. 4, 5 and S1 (Supplementary information)) clearly suggest the presence of several multi-dimensional nano to meso-scale defect features in the SiGe nanostructured matrix, such as, (i) uniformly distributed nano-porosity ~ 25-200 nm (ii) nanocrystalline grains (average grain size of ~20 nm) (iii) isolated amorphous region embedded in crystalline matrix (few nm to tens of nm) and (iv) dislocations (~ few nm). These multi dimensional defect features in a range of atomic, nano and meso-scale can effectively scatter low-to-high wavelength phonons thus leading to a significant reduction in κ_L. While atomic scale defects like, point defect are due to alloying, the dislocations and isolated amorphous regions arise due to extended hours of HEBM.[74, 75] These atomic sized point defects and dislocations are of the order of few nm and thus can effectively scatter short-wavelength phonons,[3, 57] while the abundant density of nanostructured interfaces and isolated amorphous region participate in the mid-wavelength phonon scattering.[73, 76] More importantly the existence of residual porosity in our nanostructured SiGe alloy, as shown in Fig. 4, was primarily due to the fast heating rates and short sintering duration of SPS, which limits the mass diffusion resulting in creation of nano to meso-scale pores.[30, 32] This residual porosity, distributed throughout in the $Si_{80}Ge_{20}$ matrix in a wide dimensional range from ~25-200 nm, act as additional scattering centers for mid-to-long wavelength range phonons,[77] in which SiGe alloys are known to conduct most of the heat through the material.[3, 4] Further, theoretical calculations on nano-porous SiGe alloys by He et al.,[30] also confirmed that the existence nano-pores can reduce the κ_L as much as by a factor of 3 - 16 depending on the scale of nano-porosity. Moreover, theoretical predictions by other researchers also concluded that large sized pores tend to strongly reduce the κ_L in $Si_{80}Ge_{20}$ alloys in contrast to Si where κ_L is reduced only when the pores are considerably smaller (< 100 nm).[32] It is well known that in TE materials, such as PbTe,[76] PbSeTe[38] and Si[28] most of the heat is transported by mid-to-long wavelength phonons,[1, 4, 78, 79] thus the meso-scale defect features are expected to play a dominant role in reducing the κ. Thus, in our nanostructured SiGe samples the nano to meso-scale residual porosity is expected to be the dominant defect features participating in the phonon scattering process thus leading to significant reduction in κ. Overall, the combined effect of scattering of heat-carrying phonons in a broad spectrum of wavelengths by different atomic (point defects and dislocations), nano (grain boundaries and isolated amorphous region) and meso-scale (residual porosity) defect features in nanostructured SiGe alloy leads to a significantly low value of κ ~ 2.04 W/mK, which is the lowest reported for p-type nanostructured $Si_{80}Ge_{20}$ alloy thus far. However, it is difficult to separate out the effect of individual atomic/nano/meso-scale defect features responsible for reduction in κ.

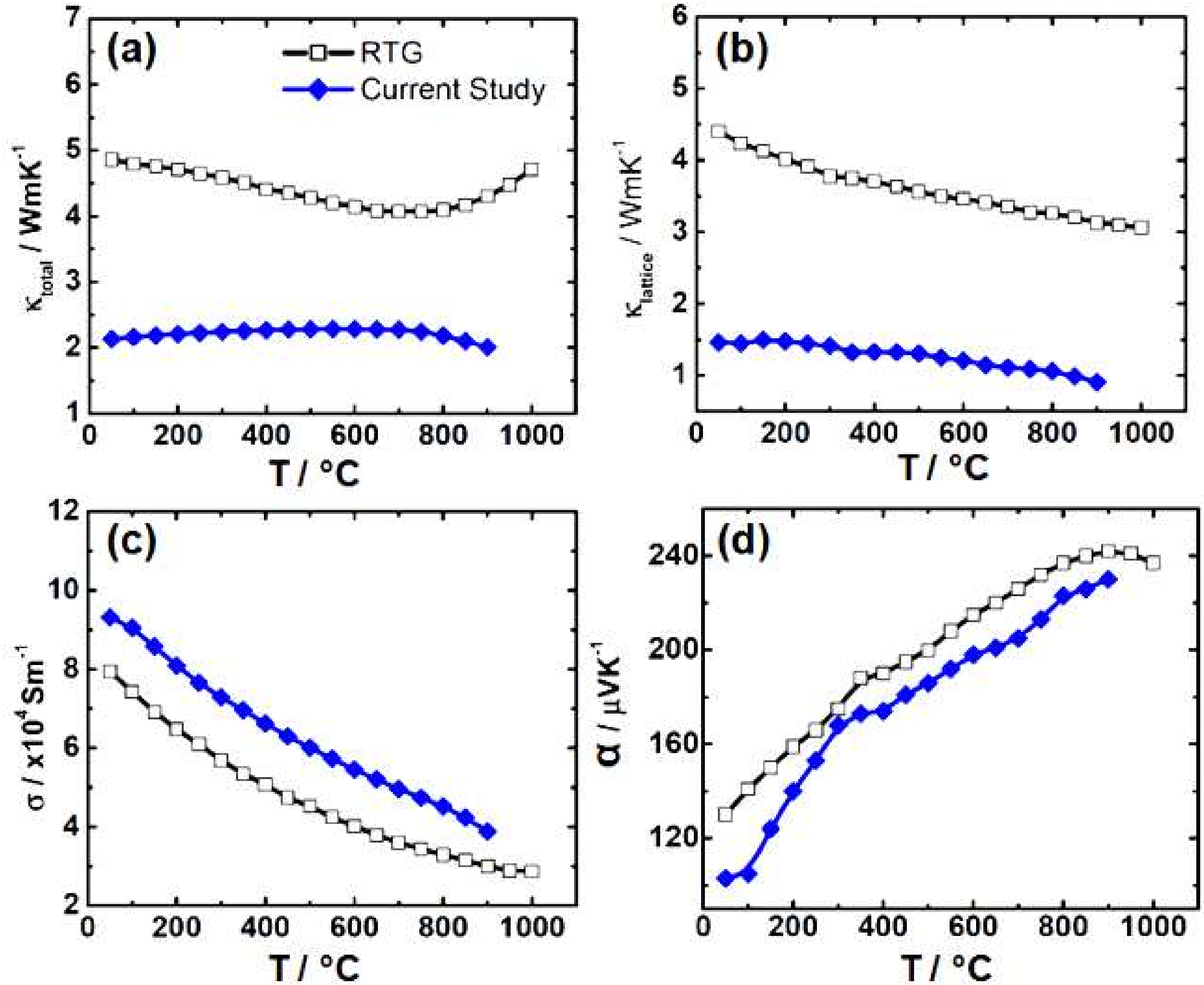

Figure 6: *(Color online)* Temperature dependence of thermoelectric properties of sintered p-type $Si_{80}Ge_{20}$ nanostructured alloys along with that reported for RTG alloy[10] (a) Total thermal conductivities (b) Lattice thermal conductivity (c) Electrical conductivity (d) Seebeck coefficient.

3. 4 Electrical transport

The temperature dependence of electrical transport properties of nanostructured $Si_{80}Ge_{20}$ alloys and RTG bulk alloy[4, 10] is shown in Fig. 6(c) and (d). It is evident from Fig. 6(c) that electrical conductivity *(σ)* of our nanostructured SiGe sample exhibits a continuous drop with temperature, which is similar to other reported studies,[4, 9, 17] although with a higher magnitude in the entire temperature range. In absolute terms, the value of *σ* was ~ 30% and ~ 35% higher (at 900°C) than reported earlier for the RTG bulk alloy[4, 10] and nanostructured $Si_{80}Ge_{20}$ alloy of similar composition,[9] respectively. This enhancement in *σ* can be attributed to the high bulk density

(98.3%) of our nanostructured $Si_{80}Ge_{20}$ sample owing to their consolidation employing SPS, which is known to yield sintered products with near-theoretical density as compared to other conventional sintering techniques, such as, hot pressing[80-82] employed by other researchers. Further, it has also been proposed[83, 84] that boron segregated at grain boundaries, goes back into the solid solution of SiGe matrix with an increase in the temperature, which results in boron diffusion into the lattice thereby creating additional charge carriers leading to an enhancement in σ. This effect is expected to be more pronounced in our nanostructured SiGe alloy samples owing to their high density of nano-scale grain boundaries.

Fig. 6(d), which shows the temperature dependence of Seebeck coefficient (α), clearly suggests that our nanostructured SiGe sample exhibits an increasing trend throughout the temperature range of measurement similar to that reported for its RTG bulk counterpart[4, 10] and nanostructured SiGe alloys,[9, 10, 16] although its magnitude is slightly lower. The magnitude of α in our nanostructured SiGe sample was found to be ~ 230 μV/K at 900ºC, which is ~10% lower than the best reported value[9] and ~ 5% lower than the bulk RTG counterpart.[4, 10] Further, the positive sign of α indicates holes as majority charge carriers thereby confirming p-type conduction in this material.

3.5 Thermoelectric performance

The calculated magnitude of the power factor ($\alpha^2\sigma$) of our nanostructured SiGe alloys (Fig. 7 (a)) was found to be ~ $2.05\text{x}10^{-3}$ $Wm^{-1}K^{-2}$ at 900°C, which is very close to that reported earlier by different researchers for nanostructured[9, 17] as well as for bulk RTG alloys[10] of similar composition. This suggests that nanostructuring in our SiGe samples results in a large reduction of thermal conductivity without significantly affecting the overall thermal transport ($\alpha^2\sigma$) especially at high temperatures, thereby suggesting a Phonon-Glass-Electron-Crystal (PGEC) kind of behavior in our nanostructured SiGe alloys.[19]

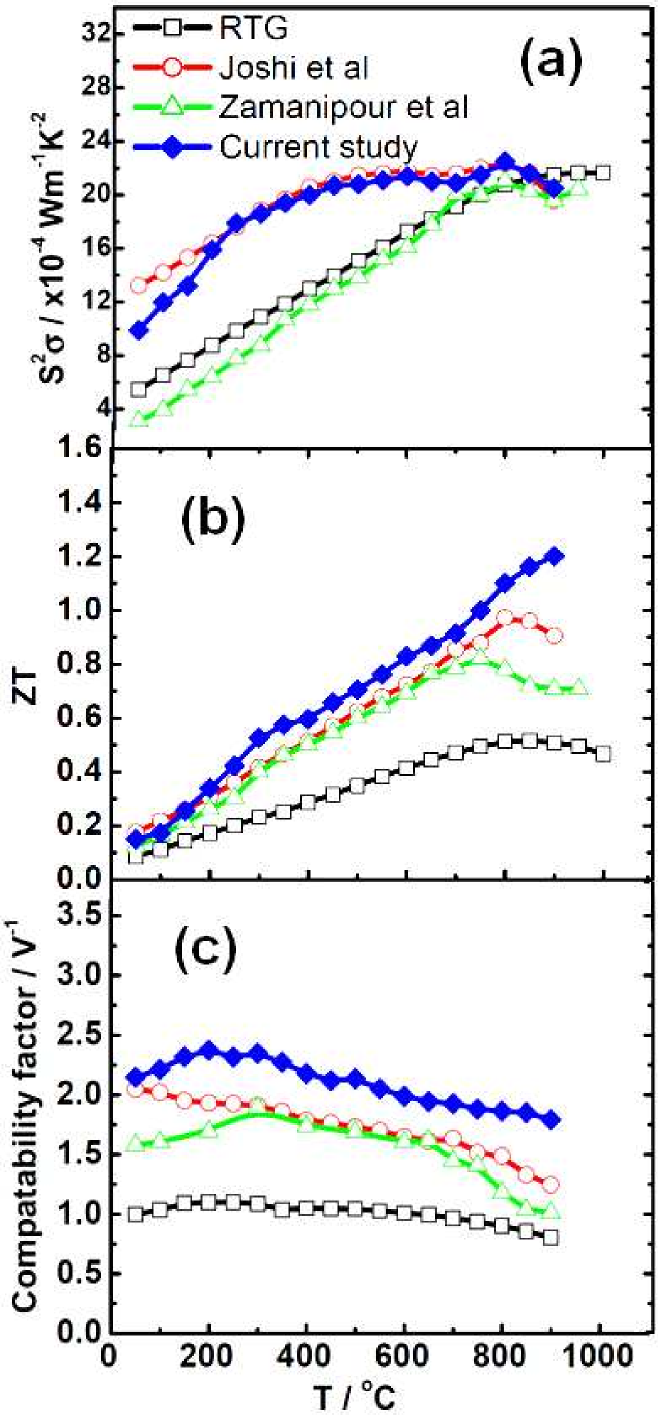

Figure 7: *(Color online)* Temperature dependence of thermoelectric properties of p-type $Si_{80}Ge_{20}$ nanostructured alloys compared with the existing reports from the literature[4, 9, 10, 16] (a) Power factor, (b) Figure-of-merit and (c) Thermoelectric compatibility factor.

After combining the results of thermal and electrical transport data, the calculated ZT as a function of temperature for our nanostructured SiGe has been shown in Fig. 7(b). In this figure, we have also included the ZT data from the existing literature[6, 85, 86] on similar p-SiGe alloys, for a direct comparison. This figure shows a high ZT ~ 1.2 at 900°C in our p-type nanostructured $Si_{80}Ge_{20}$ alloy, which is a ~ 25% enhancement over the existing state-of-the-art value[9] and ~140% higher than the conventional RTG bulk sample[4, 10] of similar composition. It is apparent from Fig.6 (a), 7(a) and 7(b) that this enhancement of ZT in our nanostructured $Si_{80}Ge_{20}$ alloy primarily originates from the reduction in its thermal conductivity, which is due to a variety of nano-to-meso scale defects participating in the phonon scattering process. The high-wavelength phonons, which are known to carry majority of heat in SiGe, are mainly scattered by the meso-scale defects (residual pores) thus leading to an enhancement of ZT due to the reduced thermal conductivity.[32, 77]

In the present study, it has been experimentally observed that the reduction in thermal conductivity, due to the residual porosity in the nanostructured SiGe matrix, not only depends on the overall porosity but also on the size of the nano-pores and their size-distribution.[32] Although, in the present work, it would have been fruitful if we could establish a direct relationship between thermal conductivity and the residual porosity in nanostructured SiGe, however, it has been experimentally observed that the inter-dependence of the overall porosity, average pore-size and their size-distribution on the variation of volume fraction of stearic acid in nanostructured SiGe matrix, is very complex. The aim of the present study is to establish, as a proof-of-principle, the well known result from several theoretical studies on TE materials,[30, 32, 87] including SiGe,[10, 30] that the thermal conductivity can significantly be reduced by incorporating nano-to-meso scale porosity[30, 77] (which is of the order of the high-wavelength phonons), in the SiGe matrix, thus leading to an enhancement in ZT.

Thermal stability studies on our nanostructured p-SiGe alloys were carried out by repeated thermal cycling between room temperature and 900°C and measuring the thermal and electrical transport properties during each thermal scan. These measurements were done over 20 thermal cycles and the reproducibility in their thermoelectric properties was found to be quite reasonable and within the experimental error (*Supplementary Information, Fig. S3)*. Similar thermal stability tests on n and p-type nanostructured SiGe alloys have also been earlier reported by Cook et al.,[88] Joshi et al.[9] and later Sivaiah et al.[15] by heat-treatment of their nanostructured SiGe alloys at 1100°C for 7 days in air and no noticeable thermoelectric property degradation or grain growth was observed under these conditions. It may be noted that the enhancement of ZT in our nanostructured p-type SiGe alloys is primarily due to their ultralow thermal conductivity ~ 2.04 W/mK at 900°C, owing to the scattering of low-to-high wavelength heat-carrying phonons by different types of defect features, in a range of nano to meso-scale dimensions, in our nanostructured $Si_{80}Ge_{20}$ alloy. Apart from the enhanced thermoelectric performance of TE materials, it is well known that in order to enhance their efficiency of TE devices segmentation of TE elements is desirable,[89, 90] which is judged by the TE compatibility factor of the material given as,[89]

$$S = \frac{\sqrt{1+ZT}-1}{\alpha T}$$

Where α is Seebeck coefficient in Volts, T is temperature in Kelvin. However, in order to derive a maximum benefit of segmentation for increasing the TE efficiency the difference in compatibility factor for the two TE materials should be less than a factor of 2.[89] Thus for designing efficient SiGe-based TE devices employing segmentation, apart from ZT, the magnitude of compatibility factor is equally important. Amongst all the exiting state-of-the-art p-type TE materials, SiGe is known to possess one of the lowest reported compatibility factor[91] rendering it rather incompatible for segmentation thereby limiting its thermoelectric efficiency.

Figure 7(c) shows the temperature dependence of the TE compatibility factor of our p-type nanostructured SiGe alloys compared with other reported studies on similar[91] alloy. It is apparent from this figure that our p-type nanostructured SiGe alloy sample shows a higher value of compatibility factor, over the entire temperature range, compared to other reported studies for the same composition. This figure suggest that typically at 400°C, the value of the compatibility factor for our nanostructured SiGe alloy ~ 2.35 V^{-1} as compared to ~ 1.8 V^{-1} which is the best reported thus far on alloys of similar composition[9]. However, most of the high ZT state-of-the-art TE materials have a compatibility factor in the range of 2.5 - 3.5[91] at 400ºC, which suggests that our nanostructured p-SiGe alloys are more amenable for segmentation and would lead to much higher efficiencies in SiGe based TE devices. Owing to their enhanced TE performance, in terms of high ZT and enhanced compatibility factor, our p-type nanostructured SiGe alloys could be potential materials for their application in RTGs, replacing the conventional SiGe bulk alloys.[10]

Conclusions

We report a significant enhancement in ZT ~ 1.2 at 900ºC in nanostructured p-type $Si_{80}Ge_{20}$ alloy synthesized employing spark plasma sintering of mechanically alloyed nanopowders. This enhancement of ZT is primarily due to its ultralow thermal conductivity ~ 2.04 W/mK at 900ºC, which owes it origin to the scattering of low-to-high wavelength heat-carrying phonons by different types of nano to meso-scale multi-dimensional defect features in $Si_{80}Ge_{20}$ nanostructured matrix. These defect features, which were characterized using FESEM, HRTEM, include point defects, dislocations, isolated amorphous regions, grain boundaries and the residual porosity distributed throughout the $Si_{80}Ge_{20}$ matrix. The nanostructured SiGe alloys also show a substantial increase in the thermoelectric compatibility factor, which coupled with an enhanced

ZT opens-up a new direction for designing segmented SiGe based thermoelectric devices with improved efficiency, primarily for RTG applications.

Acknowledgements

This work was supported by CSIR-TAPSUN (NWP-54) programme entitled *"Novel approaches for solar energy conversion under technologies and products for solar energy utilization through networking"*. The authors are grateful to Mr. Radhey Shyam and Mr. N. K. Upadhyay for their technical and experimental support.

References

1. G. J. Snyder and E. S. Toberer, *Nature Materials*, 2008, 7, 105-114.
2. B. Poudel, Q. Hao, Y. Ma, Y. Lan, A. Minnich, B. Yu, X. Yan, D. Wang, A. Muto and D. Vashaee, *Science*, 2008, 320, 634-638.
3. D. M. Rowe, *Thermoelectrics handbook: macro to nano*, CRC press, 2005.
4. D. M. Rowe, *CRC handbook of thermoelectrics*, CRC press, 1995.
5. S. Fan, J. Zhao, J. Guo, Q. Yan, J. Ma and H. H. Hng, *Applied Physics Letters*, 2010, 96, 182104-182104-182103.
6. H. Liu, X. Shi, F. Xu, L. Zhang, W. Zhang, L. Chen, Q. Li, C. Uher, T. Day and G. J. Snyder, *Nature materials*, 2012, 11, 422-425.
7. X. Shi, J. Yang, J. R. Salvador, M. Chi, J. Y. Cho, H. Wang, S. Bai, J. Yang, W. Zhang and L. Chen, *Journal of the American Chemical Society*, 2011, 133, 7837-7846.
8. M. Ito, T. Tada and S. Katsuyama, *Journal of Alloys and Compounds*, 2003, 350, 296-302.
9. G. Joshi, H. Lee, Y. Lan, X. Wang, G. Zhu, D. Wang, R. W. Gould, D. C. Cuff, M. Y. Tang and M. S. Dresselhaus, *Nano letters*, 2008, 8, 4670-4674.
10. C. B. Vining, W. Laskow, J. O. Hanson, R. R. Van der Beck and P. D. Gorsuch, *Journal of applied physics*, 1991, 69, 4333-4340.
11. S. R. Brown, S. M. Kauzlarich, F. Gascoin and G. J. Snyder, *Chemistry of Materials*, 2006, 18, 1873-1877.
12. E. S. Toberer, M. Christensen, B. B. Iversen and G. J. Snyder, *Physical Review B*, 2008, 77, 075203.
13. S. R. Culp, S. J. Poon, N. Hickman, T. M. Tritt and J. Blumm, *Applied Physics Letters*, 2006, 88, 042106-042106-042103.
14. G. L. Bennett, 2006.
15. S. Bathula, M. Jayasimhadri, N. Singh, A. Srivastava, J. Pulikkotil, A. Dhar and R. Budhani, *Applied Physics Letters*, 2012, 101, 213902.
16. Z. Zamanipour and D. Vashaee, *Journal of Applied Physics*, 2012, 112, 093714.
17. Z. Zamanipour, X. Shi, A. M. Dehkordi, J. S. Krasinski and D. Vashaee, *Physica Status Solidi (a)*, 2012, 209, 2049-2058.
18. A. Zhou, X. Zhao, T. Zhu, S. Yang, T. Dasgupta, C. Stiewe, R. Hassdorf and E. Mueller, *Materials Chemistry and Physics*, 2010, 124, 1001-1005.
19. M. S. Dresselhaus, G. Chen, M. Y. Tang, R. Yang, H. Lee, D. Wang, Z. Ren, J. P. Fleurial and P. Gogna, *Advanced Materials*, 2007, 19, 1043-1053.
20. O. Guillon, J. Gonzalez-Julian, B. Dargatz, T. Kessel, G. Schierning, J. Räthel and M. Herrmann, *Advanced Engineering Materials*, 2014.
21. K. Nielsch, J. Bachmann, J. Kimling and H. Böttner, *Advanced Energy Materials*, 2011, 1, 713-731.
22. G. Joshi, X. Yan, H. Wang, W. Liu, G. Chen and Z. Ren, *Advanced Energy Materials*, 2011, 1, 643-647.
23. S. Chen, K. C. Lukas, W. Liu, C. P. Opeil, G. Chen and Z. Ren, *Advanced Energy Materials*, 2013, 3, 1210-1214.
24. J. Yang, H. L. Yip and A. K. Y. Jen, *Advanced Energy Materials*, 2013, 3, 549-565.
25. C. Melis and L. Colombo, *Physical review letters*, 2014, 112, 065901.
26. S. K. Bux, R. G. Blair, P. K. Gogna, H. Lee, G. Chen, M. S. Dresselhaus, R. B. Kaner and J. P. Fleurial, *Advanced Functional Materials*, 2009, 19, 2445-2452.
27. W. Xie, J. He, H. J. Kang, X. Tang, S. Zhu, M. Laver, S. Wang, J. R. Copley, C. M. Brown and Q. Zhang, *Nano Letters*, 2010, 10, 3283-3289.

28. G. Zhu, H. Lee, Y. Lan, X. Wang, G. Joshi, D. Wang, J. Yang, D. Vashaee, H. Guilbert and A. Pillitteri, *Physical Review Letters*, 2009, 102, 196803.
29. C. J. Vineis, A. Shakouri, A. Majumdar and M. G. Kanatzidis, *Advanced Materials*, 2010, 22, 3970-3980.
30. Y. He, D. Donadio and G. Galli, *Nano letters*, 2011, 11, 3608-3611.
31. J.-H. Lee, G. A. Galli and J. C. Grossman, *Nano letters*, 2008, 8, 3750-3754.
32. C. Bera, N. Mingo and S. Volz, *Physical review letters*, 2010, 104, 115502.
33. J.-H. Lee and J. C. Grossman, *Applied Physics Letters*, 2009, 95, 013106.
34. W.-Y. Zhao, Z. Liang, P. Wei, J. Yu, Q.-J. Zhang and G.-S. Shao, *Acta materialia*, 2012, 60, 1741-1746.
35. Z. Zhang, P. A. Sharma, E. J. Lavernia and N. Yang, *Journal of Materials Research*, 2011, 26, 475-484.
36. Y. Zhang, G. Xu, F. Han, Z. Wang and C. Ge, *Journal of electronic materials*, 2010, 39, 1741-1745.
37. B. Gahtori, S. Bathula, K. Tyagi, M. Jayasimhadri, A. Srivastava, S. Singh, R. Budhani and A. Dhar, *Nano Energy*, 2015.
38. Q. Hao, G. Zhu, G. Joshi, X. Wang, A. Minnich, Z. Ren and G. Chen, *Applied Physics Letters*, 2010, 97, 063109.
39. C. B. Vining, *Journal of Applied Physics*, 1991, 69, 331-341.
40. K. Biswas, J. He, I. D. Blum, C.-I. Wu, T. P. Hogan, D. N. Seidman, V. P. Dravid and M. G. Kanatzidis, *Nature*, 2012, 489, 414-418.
41. J. He, M. G. Kanatzidis and V. P. Dravid, *Materials Today*, 2013, 16, 166-176.
42. R. Chaim, R. Marder, C. Estournés and Z. Shen, *Advances in Applied Ceramics*, 2012, 111, 280-285.
43. S. Bathula, R. Anandani, A. Dhar and A. Srivastava, *Materials Science and Engineering: A*, 2012, 545, 97-102.
44. G. Yamamoto, M. Omori, T. Hashida and H. Kimura, *Nanotechnology*, 2008, 19, 315708.
45. A. Minnich, M. Dresselhaus, Z. Ren and G. Chen, *Energy & Environmental Science*, 2009, 2, 466-479.
46. Z. Zhang, J. K. Yee, P. A. Sharma, N. Yang and E. J. Lavernia, *Journal of Materials Research*, 2013, 28, 1853-1861.
47. Z. Zamanipour, E. Salahinejad, P. Norouzzadeh, J. S. Krasinski, L. Tayebi and D. Vashaee, *Journal of Applied Physics*, 2013, 114, 023705.
48. D. L. Harame, 2006.
49. B. D. Cullity, *American Journal of Physics*, 1957, 25, 394-395.
50. S. Bathula, B. Gahtori, M. Jayasimhadri, S. Tripathy, K. Tyagi, A. Srivastava and A. Dhar, *Applied Physics Letters*, 2014, 105, 061902.
51. R. Orru, R. Licheri, A. M. Locci, A. Cincotti and G. Cao, *Materials Science and Engineering: R: Reports*, 2009, 63, 127-287.
52. J. H. Chae, K. H. Kim, Y. H. Choa, J.-i. Matsushita, J.-W. Yoon and K. B. Shim, *Journal of Alloys and Compounds*, 2006, 413, 259-264.
53. H. Zhang, M.-B. Tang, W. Schnelle, M. Baitinger, Z.-Y. Man, H.-H. Chen, X.-X. Yang, J.-T. Zhao and Y. Grin, *Journal of Electronic Materials*, 2010, 39, 1772-1776.
54. Q. Zhang, Q. Zhang, S. Chen, W. Liu, K. Lukas, X. Yan, H. Wang, D. Wang, C. Opeil and G. Chen, *Nano Energy*, 2012, 1, 183-189.
55. C.-H. Kuo, C.-S. Hwang, M.-S. Jeng, W.-S. Su, Y.-W. Chou and J.-R. Ku, *Journal of alloys and compounds*, 2010, 496, 687-690.
56. T. Harman, M. Walsh and G. Turner, *Journal of Electronic Materials*, 2005, 34, L19-L22.

57. G. S. Nolas, J. Poon and M. Kanatzidis, *MRS bulletin*, 2006, 31, 199-205.
58. R. M. Davis and C. Koch, *Scripta metallurgica*, 1987, 21, 305-310.
59. C. Bhandari and D. Rowe, *Journal of Physics C: Solid State Physics*, 1978, 11, 1787.
60. N. Savvides and H. Goldsmid, *Journal of Physics C: Solid State Physics*, 1973, 6, 1701.
61. C. T. Walker and R. O. Pohl, *Physical Review*, 1963, 131, 1433-1442.
62. J. Zou, D. Kotchetkov, A. A. Balandin, D. I. Florescu and F. H. Pollak, *Journal of applied physics*, 2002, 92, 2534-2539.
63. P. Carruthers, *Reviews of Modern Physics*, 1961, 33, 92-138.
64. G. Chen and H. Lou, *Oxidation of Metals*, 2000, 54, 155-162.
65. D. Morelli, J. Heremans and G. Slack, *Physical Review B*, 2002, 66, 195304.
66. A. R. Regel, I. A. Smirnov and E. V. Shadrichev, *Journal of Non-Crystalline Solids*, 1972, 8–10, 266-271.
67. G. Mahan and M. Bartkowiak, *Applied Physics Letters*, 1999, 74, 953-954.
68. P. F. Poudeu, J. D'Angelo, H. Kong, A. Downey, J. L. Short, R. Pcionek, T. P. Hogan, C. Uher and M. G. Kanatzidis, *Journal of the American Chemical Society*, 2006, 128, 14347-14355.
69. N. Mingo, D. Hauser, N. Kobayashi, M. Plissonnier and A. Shakouri, *Nano letters*, 2009, 9, 711-715.
70. J. Garg, N. Bonini, B. Kozinsky and N. Marzari, *Physical review letters*, 2011, 106, 045901.
71. Y. K. Koh and D. G. Cahill, *Physical Review B*, 2007, 76, 075207.
72. E. Steigmeier and B. Abeles, *Physical Review*, 1964, 136, A1149.
73. D. Rowe, V. Shukla and N. Savvides, 1981.
74. S. Baker, Y.-C. Joo, M. Knauss and E. Arzt, *Acta materialia*, 2000, 48, 2199-2208.
75. D. Elliott, *Geological Society of America Bulletin*, 1973, 84, 2645-2664.
76. Z.-G. Chen, G. Han, L. Yang, L. Cheng and J. Zou, *Progress in Natural Science: Materials International*, 2012, 22, 535-549.
77. H. Lee, D. Vashaee, D. Wang, M. S. Dresselhaus, Z. Ren and G. Chen, *Journal of Applied Physics*, 2010, 107, 094308.
78. G. Chen, *International journal of thermal sciences*, 2000, 39, 471-480.
79. W. Kim, J. Zide, A. Gossard, D. Klenov, S. Stemmer, A. Shakouri and A. Majumdar, *Physical review letters*, 2006, 96, 045901.
80. M. Omori, *Materials Science and Engineering: A*, 2000, 287, 183-188.
81. Z. Munir, U. Anselmi-Tamburini and M. Ohyanagi, *Journal of Materials Science*, 2006, 41, 763-777.
82. S. Wang, L. Chen and T. Hirai, *Journal of Materials Research*, 2000, 15, 982-987.
83. L. Wang and P. Clancy, *Journal of Applied Physics*, 2004, 96, 1939-1946.
84. R. Lever, J. Bonar and A. Willoughby, *Journal of Applied Physics*, 1998, 83, 1988-1994.
85. X. Xing-Xing, X. Wen-Jie, T. Xin-Feng and Z. Qing-Jie, *Chinese Physics B*, 2011, 20, 087201.
86. B. Yu, W. Liu, S. Chen, H. Wang, H. Wang, G. Chen and Z. Ren, *Nano Energy*, 2012, 1, 472-478.
87. J.-H. Lee, J. Grossman, J. Reed and G. Galli, *Applied Physics Letters*, 2007, 91, 223110-223110-223113.
88. B. Cook, J. Harringa, S. Han and C. Vining, *Journal of Applied Physics*, 1995, 78, 5474-5480.
89. G. J. Snyder and T. S. Ursell, *Physical Review Letters*, 2003, 91, 148301.
90. G. J. Snyder, *Applied Physics Letters*, 2004, 84, 2436-2438.
91. P. H. Ngan, D. V. Christensen, G. J. Snyder, L. T. Hung, S. Linderoth, N. V. Nong and N. Pryds, *Physica Status Solidi (a)*, 2014, 211, 9-17.